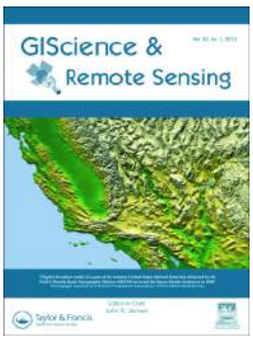

GIScience & Remote Sensing

ISSN: (Print) (Online) Journal homepage: https://www.tandfonline.com/loi/tgrs20

Comparison of spectral indices extracted from Sentinel-2 images to map plastic covered greenhouses through an object-based approach

Manuel A. Aguilar, Rafael Jiménez-Lao, Claudio Ladisa, Fernando J. Aguilar & Eufemia Tarantino

To cite this article: Manuel A. Aguilar, Rafael Jiménez-Lao, Claudio Ladisa, Fernando J. Aguilar & Eufemia Tarantino (2022) Comparison of spectral indices extracted from Sentinel-2 images to map plastic covered greenhouses through an object-based approach, GIScience & Remote Sensing, 59:1, 822-842, DOI: 10.1080/15481603.2022.2071057

To link to this article: https://doi.org/10.1080/15481603.2022.2071057

Published online: 06 May 2022.

GISCIENCE & REMOTE SENSING
2022, VOL. 59, NO. 1, 822–842
https://doi.org/10.1080/15481603.2022.2071057

Taylor & Francis
Taylor & Francis Group

Comparison of spectral indices extracted from Sentinel-2 images to map plastic covered greenhouses through an object-based approach

Manuel A. Aguilar[a], Rafael Jiménez-Lao[a], Claudio Ladisa[b], Fernando J. Aguilar[a] and Eufemia Tarantino[b]

[a]Department of Engineering and Research Centre CIAIMBITAL, University of Almería, Almería, Spain; [b]DICATECh, Politecnico di Bari, Bari, Italy

ABSTRACT

One of the most important challenges of agriculture today is increasing its productivity gains, while controlling its environmental footprint. Because of that plastic covered greenhouses (PCG) mapping via remote sensing is receiving a great attention throughout this century. In this study, a fair comparison was carried out in four PCG study areas around the world to test 14 spectral indices mainly focused on the detection of plastic. To the best knowledge of the authors, this is the first research that fairly compares all these spectral indices in such variable number of study sites. The applied OBIA approach was based on the combined use of very high-resolution satellite data (Deimos-2 pansharpened images) to address the segmentation process and Sentinel-2 time series to compute the spectral indices. When dealing with Sentinel-2 single images, the Plastic GreenHouse Index (PGHI) stood out among all the indices tested in the study areas dedicated to the cultivation of vegetables, such as the cases of Almería (Spain), Agadir (Morocco) and Antalya (Turkey). Better Overall Accuracy (OA) values of 94.09%, 92.27%, 92.77% and 92.17% were achieved for Almería, Agadir, Bari and Antalya study sites, respectively, when using statistical seasonal spectral indices based on Sentinel-2 time series, being the maximum and mean values of PGHI (MAX (PGHI) and MEAN (PGHI)) the best ranked. Meanwhile, the PCG area of Bari (Italy), with a monoculture in vineyards, presented the worst and most irregular results.

ARTICLE HISTORY
Received 16 December 2021
Accepted 22 April 2022

KEYWORDS
Plastic greenhouse; spectral indices; OBIA; segmentation; Sentinel-2; decision tree

1. Introduction

The world will require increased crop production in order to feed its predicted 9 billion people (The Royal Society 2009) by 2050. In fact, one of the most important challenges of contemporary agriculture must be to increase its productivity gains while controlling, at the same time, the agriculture's environmental footprint (Foley et al. 2011). In this way, since the first use of a plastic film in agriculture dated in 1948 (Garnaud 2000), the use of these materials as a tool to bring forward the first harvest and increase the yield of horticultural crops has been steadily increasing throughout the world (Espí et al. 2006). Two recent studies focused on the estimation of the area of permanent greenhouses (low tunnels and row covers or mulching are excluded) coincide in indicating a world area of around 500,000 ha (RaboResearch 2018; Cuesta Roble Consulting 2019). This area corresponds mainly to plastic covered greenhouses (PCG), although it also includes roughly 40,000 ha of glasshouses. The greenhouse area around the world is mainly located in China (82,000 ha), Spain (70,000 ha), Korea (51,787 ha), Italy (42,800), Turkey (42,384 ha), Morocco (20,000 ha) and Mexico (20,000 ha) (RaboResearch 2018).

However, this expansive use of plastic film in agriculture has several negative environmental effects. These include the accumulation of microplastics in the environment (Jambeck et al. 2015), mainly in soils (FAO 2021), modification of the microclimate, alteration of the distribution of pollinators, aesthetic pollution of the rural landscape (Jensen and Malter 1995; Picuno, Tortora, and Capobianco 2011), organic waste disposal problem, over-exploitation of the water resources and invasion of protected natural areas (Agüera, Aguilar, and Aguilar 2006).

A recent report by the Food and Agriculture Organization (FAO 2021) makes a loud call to coordinate good management practices and curb the disastrous use of plastics across the agricultural sector. In this sense, it is vital to develop efficient monitoring and mapping systems to control the spatiotemporal

CONTACT Manuel A. Aguilar maguilar@ual.es

changes of PCG around the world, and remote sensing can provide accurate and periodic information of this sector (Song et al. 2017).

Remote sensing have been widely applied for mapping PCG and plastic-mulched areas during the last decade, mainly using Landsat 5/7/8 image data (Lu, Di, and Ye 2014; Aguilar et al. 2015; Novelli and Tarantino 2015; Aguilar et al. 2016; Wu et al. 2016; Hasituya, and Chen 2017; Yang et al. 2017; González-Yebra et al. 2018; Hasituya et al. 2020; Ji et al. 2020; Ou et al. 2020). Other free access optical data widely used in PCG mapping in recent years are those provided by the twin polar-orbiting European satellites, Sentinel-2A and Sentinel-2B, successfully launched in 2015 and 2017, respectively (Lu, Tao, and Di 2018; Hao et al. 2019; Perilla and Mas 2019; Balcik, Senel, and Goksel 2020; Ibrahim and Gobin 2021; Sun et al. 2021). There are also works focused on comparing Sentinel-2 and Landsat 8 imagery to classify PCG (Novelli et al. 2016; Nemmaoui et al. 2018). Moreover, Xiong et al. (2019) fused Sentinel-2, Landsat 5/7/8 and MODIS imagery to propose a new framework to map plastic-mulched farmland over large areas.

New works focused on the detection of PCG from the first successfully launched very high-resolution (VHR) commercial satellites (IKONOS in 1999 and QuickBird in 2001) have been performed by using different pixel-based approaches (Agüera, Aguilar, and Aguilar 2006, 2008; Carvajal et al. 2010; Arcidiacono and Porto 2011). Koc-San (2013) used WorldView-2 satellite imagery to carry out a pixel-based classification of glass and plastic greenhouses in Antalya (Turkey). Aguilar et al. (2014) tested GeoEye-1 and WorlView-2 stereo pairs for mapping PCG in Almería (Spain) using an object-based image analysis (OBIA) approach. China's high resolution Earth Observation System satellites, GaoFen-1 (Hasituya et al. 2020) and GaoFen-2 (Shi et al. 2020), were successfully used to map PCG and plastic-mulched farmland. The potential of Pléiades data for mapping plastic-mulched farmland using OBIA and Random Forest (RF) classifier have been also reported (Hasituya et al. 2021). Without any doubt, WorldView-3 can be considered the VHR satellite that has shown the most impressive capabilities for mapping PCG thanks to its global super-spectral (eight VNIR bands and eight SWIR bands) observation capabilities (Aguilar, Jiménez-Lao, and Aguilar 2021). Finally, the deep learning framework has recently been applied to classify PCG and mulching films using VHR imagery usually downloaded from open-access sites (Feng et al. 2021; Jakab, van Leeuwen, and Zalán 2021; Ma et al. 2021). Li et al. (2020) and Zhang et al. (2021) also used deep learning to extract PCG from GaoFen-1 and GaoFen-2 images.

Several spectral indices for mapping PCG and mulching films have been proposed in this century. All these PCG indices were particularly tested for a specific study area with a certain type of PCG. For example, Zhao et al. (2004) proposed an index for greenhouse vegetable land extraction (Vi) oriented to PCG mapping in the Shandong province of China using Landsat Thematic Mapper (TM) imagery. Lu, Di, and Ye (2014) developed and included the plastic-mulched land cover index (PMLI) into a decision tree classifier from Landsat 5 TM images. Aguilar et al. (2016) tested the spectral metric Moment Distance Index (MDI) proposed by Salas and Henebry (2012), including its two components (Moment Distance from the Left Pivot (MDLP) and to the Right one (MDRP)), for mapping PCG in Almería (Spain) using an OBIA approach and Landsat 8 time series. Yang et al. (2017) developed new spectral indices (Plastic Greenhouse Index (PGI) and Retrogressive Plastic Greenhouse Index (RPGI)) for detecting PCG in Shandong (China) following a pixel-based approach. After that, González-Yebra et al. (2018) published the Greenhouse Detection Index (GDI) based on MDI index, the blue band and the two SWIR bands from Landsat images. More recently, Ji et al. (2020) developed a threshold model for mapping PCG from Landsat 8 images using an OBIA approach in Xuzhou city (Jiangsu Province, China). They proposed the Plastic GreenHouse Index (PGHI), to reject bright white buildings, and the Color Steel Buildings Index (CSBI), to discriminate the color steel buildings, within the context of PCG classification. In addition, other spectral indices have been derived from medium resolution optical satellite images for mapping plastic litter in the marine environment, which could be interesting to classify PCG. In this way, Biermann et al. (2020) proposed the Floating Debris Index (FDI), while Themistocleous et al. (2020) developed the Plastic Index (PI), both from Sentinel-2 Multi-Spectral Instrument (MSI) images.

The goal of this work relies on making a fair comparison between the aforementioned spectral indices by assessing their performance in PCG mapping

within the context of an OBIA approach. Obviously, these indices don't work in the same way in all the PCG areas around the world, nor at all times of the year. Therefore, time series of Sentinel-2 images were used in four representative PCG study sites located in different countries. The main idea is to highlight the most robust index for mapping PCG at present. Thus far, and to the best knowledge of the authors, this is the first research that compares, using the same methodology, the performance of mapping PCG in such a large number of countries.

2. Study areas

The four study sites, Spain (SS1), Morocco (SS2), Italy (SS3) and Turkey (SS4), used in this work are located in relevant and typical agricultural greenhouse areas (Figure 1(a)). All the study sites have a rectangular shape with an area of ca. 8000 ha (8,000 x 10,000 m), being the topography quite flat (Aguilar et al. 2020a).

SS1 study site, centered on the geographic coordinates (WGS84) 36.7824°N and 2.6867°W (Figure 1(b)), is located in Almería (Spain). This study area has already been studied in works focused on mapping PCG (e.g. Aguilar et al. 2016; Nemmaoui et al. 2018). The under plastic agriculture is the main key economic driver in the Almería province, being tomato, pepper, cucumber, aubergine, melon, and watermelon the most representative greenhouse horticultural crops. SS1 includes villages such as Cortijos de Marín, La Mojonera, Puebla de Vícar and La Venta del Viso. PCG plots in SS1 have no crop underneath in July, presenting very few areas of isolated vegetation.

SS2 is located in the Souss-Massa plain, in Agadir (Morocco) (geographic coordinates (WGS84) 30.1478° N and 9.4386°W) (Figure 1(c)). In this area, there are more than 10,000 ha of PCG mainly dedicated to tomato. This study site does not include any urban area. SS2 displays a few agricultural parcels with orchards and outdoor crops.

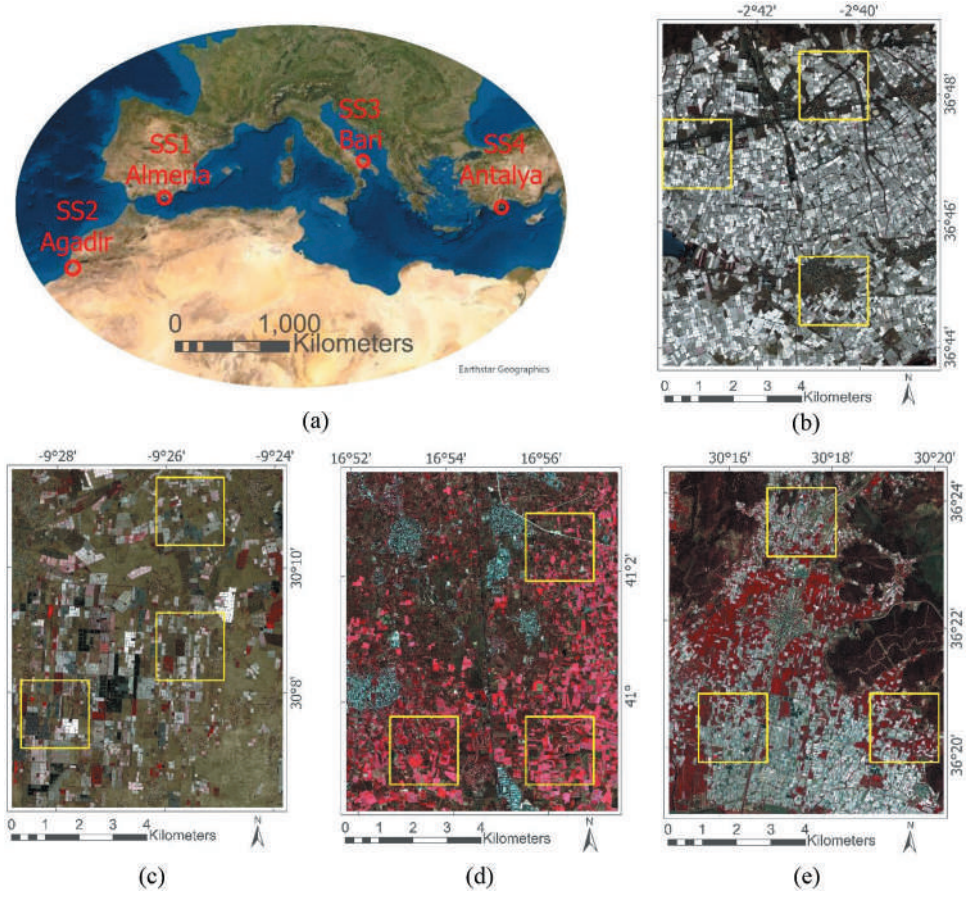

Figure 1. Global location and detailed views of the four study sites based on Near infrared, red, green false-color band combination of Deimos-2 images: (a) Global location of the four study sites (SS1: Almería (Spain); SS2: Agadir (Morocco); SS3: Bari (Italy); SS4 Antalya (Turkey); (b) SS1; (c) SS2; (d) SS3; (e) SS4. Yellow squared areas for the accuracy assessment are represented.

SS3 is situated in the Apulia Region (Italy), close to Bari (41.0166°N and 16.9119°E) (Figure 1(d)). In this study site there is a monoculture in vineyards, where it is grown using the traditional grape growing system characterized by a supporting structure covered with plastic sheets or nets in spring and summer. SS3 presents several villages such as Valenziano Apulia, Capurso, Cellamare, Parco dei Principi, Adelfia. In addition, it includes a few industrial zones. SS3 has a large area covered with vegetation in July, mainly agricultural plots with vineyards.

SS4 is located in Kumluca (Turkey), district of Antalya Province (36.3622°N and 30.2931°E). SS4 has a similar production model as SS1 and SS2, being addressed to horticultural crops growing both under PCG (80–85%) and glass greenhouses (15–20%). Several orange tree and olive tree orchards appear in red surrounding the city of Kumluca, together with a large quantity of greenhouses without crop (Figure 1(e)).

Moreover, three yellow squared areas for each study area are represented in Figure 1. They will be used later for the accuracy assessment stage.

3. Datasets and pre-processing

3.1. Deimos-2 images

Deimos-2 is a VHR optical satellite operated by Deimos Imaging. Deimos-2 was launched on 19 June 2014. It provides 1 m ground sample distance (GSD) panchromatic (PAN) and 4 m multispectral (MS) images containing four bands (R, G, B, NIR).

In this study, four Deimos-2 images (PAN+MS) level 1B (L1B) were acquired at the study sites in different dates: 30 July 2019 for SS1 (Figure 1(b)), 9 July 2020 for SS2 (Figure 1(c)), 29 July 2020 for SS3 (Figure 1(d)) and 17 July 2020 for SS4 (Figure 1(e)). The L1B product presents calibration and radiometric correction. This basic product includes the sensor camera model (RPCs) and the gain and bias values for each band.

The PANSHARP module of Geomatica v. 2018 (PCI Geomatics, Richmond Hill, ON, Canada) was used to produce the Deimos-2 pansharpened images with 1 m of GSD, containing the full four-band spectral information. According to Aguilar et al. (2020b), 12 ground control points (GCPs) are required for Deimos-2 L1B images, to compute the ideal sensor model based on rational functions refined by a first-order transformation in the image space (RPC1). For obtaining the Deimos orthoimages for each study site, freely available ancillary data of Google Earth (GCPs) and the Shuttle Radar Topography Mission 30 m digital elevation model (DEM) were used following the recommendation by Aguilar et al. (2017).

The final Deimos-2 pansharpened orthoimages were atmospherically corrected by using the ATCOR module (Berk et al. 1998) implemented in Geomatica v. 2018.

3.2. Sentinel-2 images

The widely known Sentinel-2 (S2) mission comprises a constellation of two identical satellites, Sentinel-2A (S2A) and Sentinel-2B (S2B), launched in 2015 and 2017, respectively. The images used in this work were taken by S2A and S2B MSI over the four study sites (Table 1). All the S2 images level 2A (L2A), with values expressed in surface reflectance, were freely downloaded in 2020 from the European Space Agency (ESA)-Copernicus Scientific Data Hub tool. Fourteen cloud-free multi-temporal S2 L2A scenes were taken at the Almería study site, while 15 were obtained for each of the other three study sites (Table 1). The goal was to have at least one cloud-free image for each month, and that the selected images were well distributed throughout the year. Moreover, and mainly in summer, we tried to choose S2 images taken from the orbits that left the sun on its back for minimizing the sun glint effects (Aguilar et al. 2020a). It resulted to be impossible in some study areas and we decided to choose a similar number of S2 (14–15) images for each time series. The S2 MSI sensor collects up to 13 bands, although only the four bands with 10 m GSD (B2-B, B3-G, B4-R and B8-NIR8) and the six bands with 20 m GSD (B5-RE1, B6-RE2, B7-RE3, B8a-NIR8a, B11-SWIR1 and B12-SWIR2) were used in this research.

The original S2 images were clipped according to its corresponding study area and co-registered with the reference Deimos-2 pansharpened orthoimage. The co-registration was performed for each acquisition time and study site using a first order polynomial transformation computed on 44 planimetric GCPs evenly distributed over each working area and extracted from the Deimos-2 orthoimages. Bearing in mind that the study sites were areas with a fairly flat topography, the co-registration turned out to be

Table 1. Original Sentinel-2 (S2A and S2B) L2A images used in this study for each study site.

Study Site	Date of Acquisition (D/M/Y)	Sensor	Orbit	ID Tile	Study Site	Date of Acquisition (D/M/Y)	Sensor	Orbit	ID Tile
SS1: Almería (Spain)	1/1/2020	S2A	R051	30SWF	SS2: Agadir (Morocco)	1/2/2020	S2B	R137	29RMP
	10/2/2020	S2A	R051			6/4/2020	S2B	R137	
	11/3/2020	S2A	R051			1/5/2020	S2B	R137	
	30/4/2020	S2A	R051			21/5/2020	S2B	R137	
	25/5/2020	S2B	R051			31/5/2020	S2B	R137	
	14/6/2020	S2B	R051			15/6/2020	S2A	R137	
	24/7/2020	S2B	R051			20/6/2020	S2B	R137	
	29/7/2020	S2A	R051			10/7/2020	S2B	R137	
	13/8/2020	S2B	R051			24/8/2020	S2A	R137	
	27/9/2020	S2A	R051			8/9/2020	S2B	R137	
	5/10/2020	S2B	R094			23/9/2020	S2A	R137	
	25/10/2020	S2B	R094			28/9/2020	S2B	R137	
	11/11/2020	S2B	R051			7/11/2020	S2B	R137	
	9/12/2020	S2A	R094			22/11/2020	S2A	R137	
						7/12/2020	S2B	R137	
Study Site	Date of Acquisition (D/M/Y)	Sensor	Orbit	ID Tile	Study Site	Date of Acquisition (D/M/Y)	Sensor	Orbit	ID Tile
SS3: Bari (Italy)	25/1/2020	S2B	R036	33TXF	SS4: Antalya (Turkey)	22/1/2020	S2A	R064	36STF
	9/2/2020	S2A	R036			9/2/2020	S2B	R107	
	13/3/2020	S2A	R079			7/3/2020	S2B	R064	
	17/4/2020	S2B	R079			11/4/2020	S2A	R064	
	9/5/2020	S2A	R036			6/5/2020	S2B	R064	
	28/6/2020	S2A	R036			16/5/2020	S2B	R064	
	3/7/2020	S2B	R036			25/6/2020	S2B	R064	
	23/7/2020	S2B	R036			10/7/2020	S2A	R064	
	2/8/2020	S2B	R036			25/7/2020	S2B	R064	
	12/8/2020	S2B	R036			19/8/2020	S2A	R064	
	27/8/2020	S2A	R036			3/9/2020	S2B	R064	
	7/9/2020	S2A	R036			8/9/2020	S2A	R064	
	6/10/2020	S2A	R036			28/9/2020	S2A	R064	
	31/10/2020	S2B	R036			12/11/2020	S2A	R064	
	15/11/2020	S2A	R036			2/12/2020	S2B	R064	

excellent. Nemmaoui et al. (2018) used 44 GCPs to align a pansharpened WorldView-2 orthoimage and S2 images achieving a residual offsets ranged between 3.20 m and 4.09 m in terms of planimetric root mean square error (RMSExy), similar values to those reported by Stumpf, Michéa, and Malet (2018).

4. Methodology

The methodology followed in this research for all the study sites is similar to the already applied by Aguilar et al. (2016) and Nemmaoui et al. (2018) in Almería. A flowchart describing the methodology proposed in this work is shown in Figure 2.

4.1 Segmentation

The multi-resolution (MRS) image segmentation algorithm implemented in eCognition 9.5 (Trimble, Sunnyvale, CA, USA) was used in this work. MRS is a bottom-up region-merging technique that starts with one-pixel objects and, by mean of iterative steps, smaller objects are merged into larger ones (Baatz and Schäpe 2000). The MRS is based on three main parameters: Scale, Shape and Compactness (Tian and Chen 2007). The combination of bands and their corresponding weights must be also set (eCognition 2019).

The segmentation for each study site was carried out by using the geometrically and atmospherically corrected Deimos-2 pansharpened images. Aguilar et al. (2018) performed the MRS segmentation of PCG from three orthoimages of WorldView-3 (PAN with 0.3 m GSD, MS and atmospherically corrected MS using ATCOR with 1.2 m), pointing to the MS ATCOR orthoimage as the best choice to obtain the best results.

According to Novelli et al. (2016), the bands combination for Deimos-2 pansharpened orthoimages was set to equally weighted Blue, Green and NIR bands. Scale values with increments in steps of 1.0 and Shape values ranged from 0.1 to 0.5 in steps of 0.1 were tested. Compactness was fixed to 0.5 in all cases (Nemmaoui et al. 2018). Thousands of segmentations from applying MRS

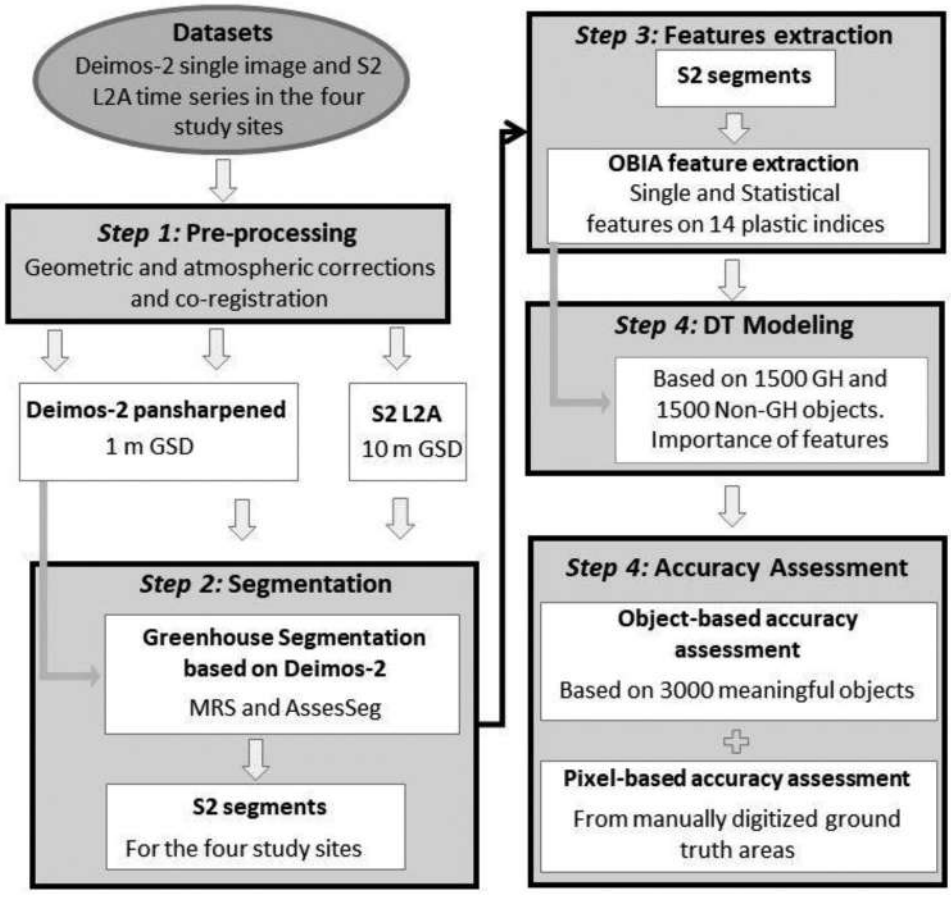

Figure 2. Flowchart of the methodology proposed in this work.

were computed by means of a semi-automatic eCognition rule set characterized by a looping process varying the aforementioned MRS tuning parameters. The selection of the best MRS parameters for each study site was carried out automatically through a free access command line tool named AssesSeg (Novelli et al. 2016, 2017). This tool is based on a modified version of the supervised discrepancy measure Euclidean Distance 2 (ED2) originally proposed by Liu et al. (2012). Four hundred reference PCG objects manually delineated on the Deimos-2 pansharpened orthoimages for each study site were considered to compute the modified ED2. Note that a high value of the modified ED2 indicates a significant geometric discrepancy between the reference and segmented PCG polygons. So, for each study site, the segmentation presenting the minimum value of ED2 was selected as the ideal.

4.2 Features extraction

Fourteen spectral indices, directly or indirectly used for mapping PCG, plastic-mulched land cover or plastic litter in the marine environment, were tested in this work (Table 2). All these indices were extracted from each S2 single image and every object attained in the segmentation process described in section 4.1. This procedure was applied to each study site using eCognition v. 9.5.

In a nutshell, object-based features were extracted from single S2 images but working on Deimos-2-based segmentation. It is important to note that the original spatial resolution of 10 m or 20 m GSD of the S2 bands were increased to 1 m by applying a spatial resampling without interpolation in order to better match the previously segmented objects on Deimos-2. One different eCognition project was conducted for each study site.

Lastly, simple statistical seasonal features corresponding to each index shown in Table 2 were also computed from the 14 or 15 images of the S2 time series for each

Table 2. Spectral indices based on Sentinel-2 single images tested for mapping PCG.

Index	Description	Reference
Normalized Difference Vegetation Index (NDVI)	$NDVI = \frac{(NIR8 - R)}{(NIR8 + R)}$	Rouse et al. (1973)
Normalized Difference Builtup Index (NDBI)	$NDBI = \frac{(SWIR1 - NIR8)}{(SWIR1 + NIR8)}$	Zha, Gao, and Ni (2003)
Moment Distance from the Right Pivot (MDRP)	$MDRP = \sum_{i=\lambda_{RP}}^{\lambda_{LP}} \sqrt{(\rho_i^2 + (\lambda_{RP} - i)^2)}$ λ = wavelength in μm; ρ = reflectance; i = 10 bands	Salas and Henebry (2012)
Moment Distance from the Left pivot (MDLP)	$MDLP = \sum_{i=\lambda_{LP}}^{\lambda_{RP}} \sqrt{(\rho_i^2 + (i - \lambda_{LP})^2)}$ λ = wavelength in μm; ρ = reflectance; i = 10 bands	Salas and Henebry (2012)
Moment Distance Index (MDI)	$MDI = MDRP - MDLP$	Salas and Henebry (2012)
Plastic-Mulched Landcover Index (PMLI)	$PMLI = \frac{SWIR1 - R}{SWIR1 + R}$	Lu, Di, and Ye (2014)
Index Greenhouse Vegetable Land Extraction (Vi)	$Vi = \left(\frac{SWIR1 - NIR8}{SWIR1 + NIR8}\right) \times \left(\frac{NIR8 - R}{NIR8 + R}\right)$	Zhao et al. (2004)
Plastic Greenhouse Index (PGI)	$PGI = 100 \times \left(\frac{B \times (NIR8 - R)}{1 - \frac{(B + G + NIR8)}{3}}\right)$ PGI = 0 when NDVI > 0.73; PGI = 0 when NDBI > 0.005	Yang et al. (2017)
Retrogressive Plastic Greenhouse Index (RPGI)	$PGI = 100 \times \left(\frac{B}{1 - \frac{(B + G + NIR8)}{3}}\right)$	Yang et al. (2017)
Greenhouse Detection Index (GDI)	$GDI = \left(\frac{MDI}{3}\right) - \left(\frac{B - \left(\frac{SWIR1 + SWIR2}{2}\right)}{B + \left(\frac{SWIR1 + SWIR2}{2}\right)}\right)$	González-Yebra et al. (2018)
Plastic GreenHouse Index (PGHI)	$PGHI = \frac{B}{SWIR2}$	Ji et al. (2020)
Color Steel Buildings Index (CSBI)	$CSBI = \frac{SWIR2}{SWIR1}$	Ji et al. (2020)
Plastic Index (PI)	$PI = \frac{NIR8}{NIR8 + R}$	Themistocleous et al. (2020)
Floating Debris Index (FDI)	$FDI = NIR8 - \left(RE2 + (SWIR1 - RE2) \times \left(\frac{\lambda_{NIR} - \lambda_{RED}}{\lambda_{SWIR1} - \lambda_{RED}}\right) \times 10\right)$ λ_{NIR} =833 nm; λ_{RED} =665 nm; λ_{SWIR1} =1613 nm	Biermann et al. (2020)

study site. Those seasonal features were MAX (maximum), MIN (minimum), DIF (difference between MAX and MIN), SD (standard deviation) and MEAN values. In that way and for instance, the value of MAX (PGHI) in Almeria for a specific object, would be the maximum value of the 14 mean PGHI values computed for this object and for each S2 image. The use of seasonal features minimized the influence of the composition of the time series (i.e. the number of images and their distribution throughout the year).

4.3. Decision tree modeling

A simple decision tree (DT) classifier based on the algorithm proposed by Breiman et al. (1984) was used in this work to assign the classes Greenhouse (GH) or Non-Greenhouse (Non-GH) to the objects. This very simple classifier with a few splits and single threshold values is ideal to compare and understand the behavior of the indices tested here. It was already selected for mapping outdoor crops by Peña-Barragan et al. (2011) and Vieira et al. (2012), even for plastic-mulched land cover detection (Lu, Di, and Ye 2014). For each study site, 1500 GH and 1500 Non-GH meaningful objects were selected as ground truth from the ideal segmentations. It is important to note that all the 1500 GH objects selected were always PCG. In Antalya (SS4) we were very careful not to mistakenly choose any glass greenhouse, even using Street View by Google Earth, since the detection of glass greenhouses was beyond the scope of this work.

STATISTICA v. 10 (StatSoft Inc., Tulsa, OK, USA) and the Gini index (Zambon et al. 2006) were used to compute DT models through a stratified 10-fold cross-validation procedure, being the dependent variable the classes GH or Non-GH. This well-kown experimental design led to one confusion matrix for each fold (Vieira et al. 2012; Peña-Barragán et al. 2014). In 10-fold cross-validation, the data is randomly partitioned into 10 equal size samples. Of the 10 samples, a single sample is used to validate the model (this sample results independent to the others) and the remaining 9 samples are used as to train the model. The cross-validation process is then repeated 10 times, with each of the 10 samples used exactly once as the validation data. A final confusion matrix was obtained by summing all of them. It is important to note that DT also provides an assessment of the

relative importance of the different features considered to carry out the classification process, which will help us to rank the tested spectral indices according to their capability to classify PCG.

For each study site, a DT was individually computed for each S2 single image, considering two classes (GH and Non-GH) and a feature vector composed of 14 features (spectral indices). In addition, a new DT was attained exclusively using the aforementioned five statistical seasonal features (14 × 5 = 70 features for each study site). These computed DTs were implemented in eCognition by means of rule sets to classify the objects previously obtained in the segmentation step.

4.4. Classification accuracy assessment

All the computed DT models (based on single image or statistical features) resulted in the corresponding confusion matrices based on the 3000 aforementioned objects (see section 4.3). These first accuracy results can be considered as an object-based accuracy assessment.

In addition, and for each study area, three squared ground truth areas of 2000 m per 2000 m were manually digitized as vector files over the Deimos-2 pansharpened orthoimage containing the two class objects (see yellow squares in Figure 1). It should be noted that a farmland was digitized as GH in the ground truth if it was interpreted as GH in at least one of the S2 images of the time series. In fact, there were some agricultural parcels included in the GH class that only appeared covered in plastic in one or two images of the time series. These squared areas were exported as raster files with 1 m GSD and finally uploaded as TTA (Test and Training Area) mask into the corresponding eCognition project to be considered as reference (ground truth). This procedure was only carried out for the strategy that used statistical seasonal features. In this way, several pixel-based sets of confusion matrices were attained to perform a more real classification accuracy assessment (Aguilar et al. 2016; Nemmaoui et al. 2018; Aguilar, Jiménez-Lao, and Aguilar 2021).

For the two accuracy assessments performed, user's accuracy for both GH and Non-GH classes (UA GH and UA Non-GH), producer's accuracy for both GH and Non-GH classes (PA GH and PA Non-GH), overall accuracy (OA), and kappa coefficient (Kappa) were measured (Congalton 1991). In the case of the accuracy based on TTA mask (pixel-based approach), an analysis of variance (ANOVA) was carried out to detect statistical significant differences. The Tukey's post hoc test with 95% confidence level was applied for means separation.

5. Results

5.1 Segmentation

The optimal setting parameters achieved for MRS segmentations (i.e. SP and Shape because Compactness was set at 0.5) carried out on equally weighted Blue-Green-NIR bands from Deimos-2 pansharpened orthoimages were the following: (i) 237, 0.4 for SS1, (ii) 192, 0.5 for SS2, (iii) 162, 0.5 for SS3, and (iv) 134, 0.5 for SS4. The modified ED2 metric (Novelli et al. 2016) used to find the optimal setting on each study site presented values of 0.299, 0.372, 0.122 and 0.213 for SS1, SS2, SS3 and SS4, respectively. The optimal MRS yielded 11,383 (SS1), 7,290 (SS2), 12,997 (SS3) and 18,489 (SS4) objects in each study area. Figure 3 shows detailed views of the ideal segmentations obtained using zone 1 (the northernmost yellow squared areas in Figure 1) of each study area (Deimos-2 pansharpened orthoimages) as a reference. All these segmentations presented a very good visual agreement with PCG shapes.

It is important to highlight that a few PCG in each study area were changing the plastic roof when Deimos-2 images were taken in July. In these cases, we verified that the agricultural plots were still well represented by MRS segmentations, since the terrain resulted to be quite homogeneous.

5.2 Relative importance of the tested spectral indices

The relative importance values of the 14 spectral indices tested on S2 single images (Table 2) derived from the DT models are shown in Table 3. These values, computed for each of the four study sites,

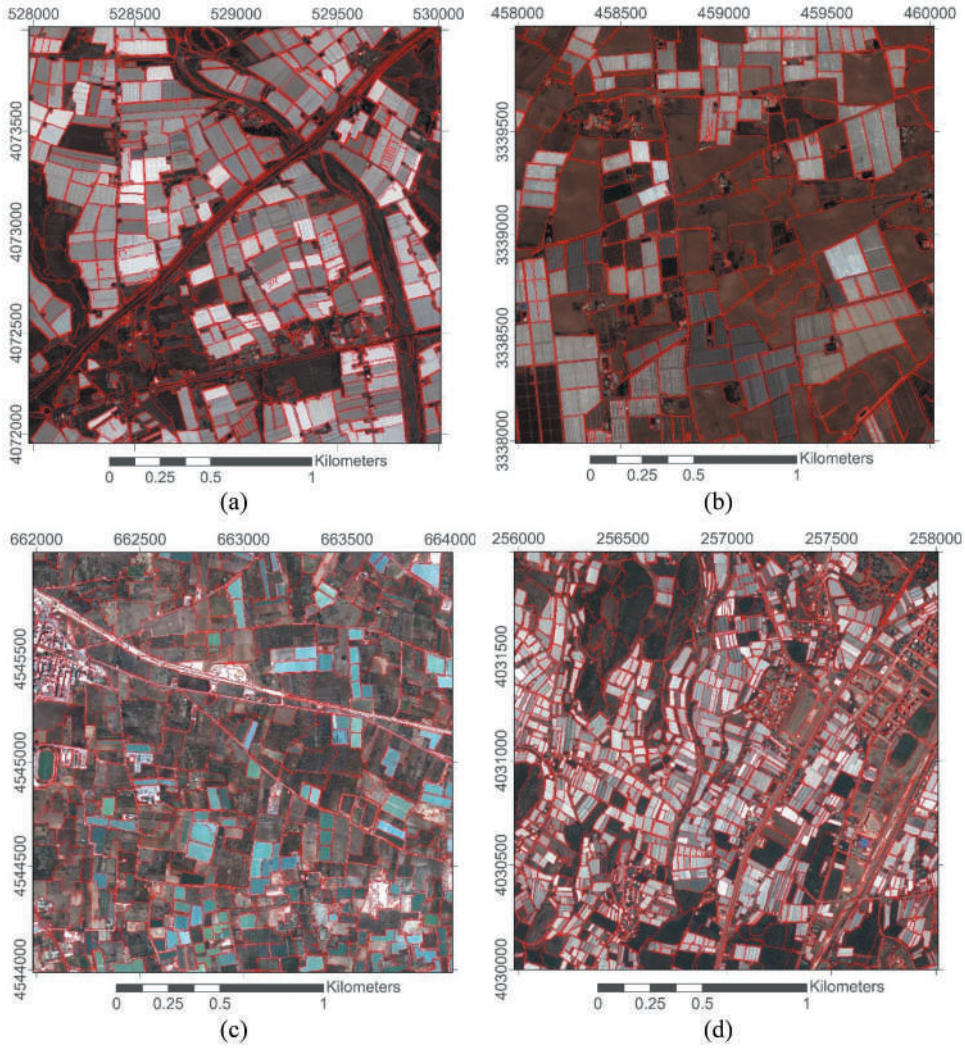

Figure 3. Detailed views (zone 1 areas) of ideal segmentations achieved on Deimos-2 pansharpened orthoimages using MRS and the modified Euclidean Distance 2 (ED2) for the four study sites: (a) SS1, Almería; (b) SS2, Agadir; (c) SS3, Bari); (d) SS4, Antalya.

Table 3. Relative importance of the spectral indices tested on S2 single images for each study site. The mean value for the four study sites is depicted in the last column.

	SS1 (Almería)	SS2 (Agadir)	SS3 (Bari)	SS4 (Antalya)	Mean value
Index	Relative importance				
PGHI	1.00	1.00	0.56	1.00	0.89
GDI	0.94	0.92	0.51	0.99	0.84
MDI	0.82	0.70	0.54	0.91	0.74
PMLI	0.84	0.72	0.41	0.93	0.72
RPGI	0.82	0.69	0.41	0.94	0.72
FDI	0.84	0.65	0.73	0.58	0.70
CSBI	0.55	0.84	0.91	0.27	0.64
NDBI	0.80	0.82	0.72	0.22	0.64
MDLP	0.69	0.44	0.48	0.83	0.61
Vi	0.51	0.81	0.75	0.25	0.58
PGI	0.54	0.37	0.73	0.42	0.51
NDVI	0.40	0.20	0.62	0.75	0.49
PI	0.40	0.20	0.62	0.75	0.49
MDRP	0.39	0.26	0.31	0.59	0.39

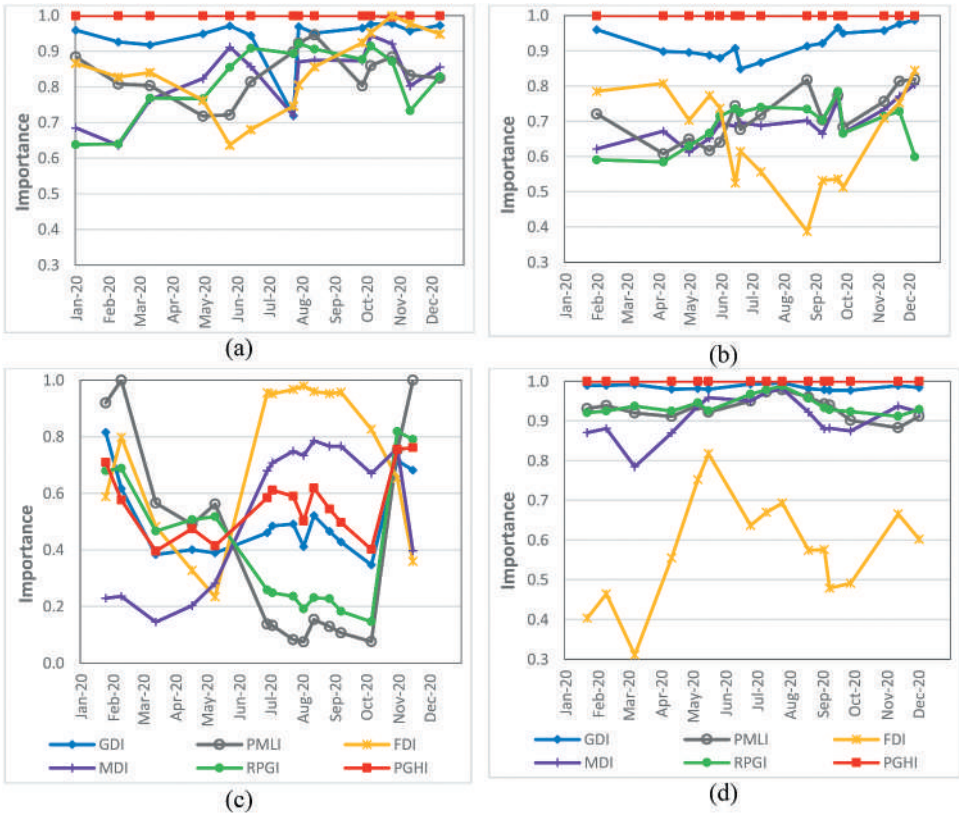

Figure 4. The top six global indices for S2 single images ranked according to their relative importance: (a) SS1, Almería; (b) SS2, Agadir; (c) SS3, Bari; (d) SS4, Antalya.

were obtained by averaging the relative importance of each spectral index through the 14 or 15 single images. Note that the ranking is ordered according to the mean values for all study sites showing in the last column.

The results regarding the relative importance of the tested spectral indices turned out to be quite similar in the three study sites devoted to growing vegetables (i.e. SS1, SS2 and SS4), PGHI and GDI being the most prominent indices, closely followed

Table 4. Relative importance of the best 14 statistical indices tested on the time series of S2 images for each study site. The mean value for the four study sites is depicted in the last column.

	SS1 (Almería)	SS2 (Agadir)	SS3 (Bari)	SS4 (Antalya)	Mean value
Index	Relative importance				
SD (PGI)	1.00	0.90	1.00	0.92	0.96
DIF (PGI)	0.99	0.90	0.99	0.83	0.93
MAX (PGHI)	0.97	0.99	0.66	1.00	0.90
DIF (PGHI)	0.92	0.91	0.89	0.86	0.89
SD (PGHI)	0.92	0.92	0.89	0.77	0.87
MIN (GDI)	0.95	0.95	0.57	1.00	0.87
SD (CSBI)	0.93	0.80	0.93	0.79	0.86
DIF (CSBI)	0.91	0.80	0.93	0.78	0.86
MIN (MDI)	0.91	0.82	0.69	0.99	0.85
MEAN (PGHI)	0.98	1.00	0.40	1.00	0.84
MIN (PGI)	0.73	0.81	0.98	0.83	0.84
MIN (PMLI)	0.93	0.94	0.37	0.99	0.81
DIF (MDI)	0.60	0.78	0.85	0.98	0.80
DIF (MDLP)	0.85	0.70	0.69	0.96	0.80

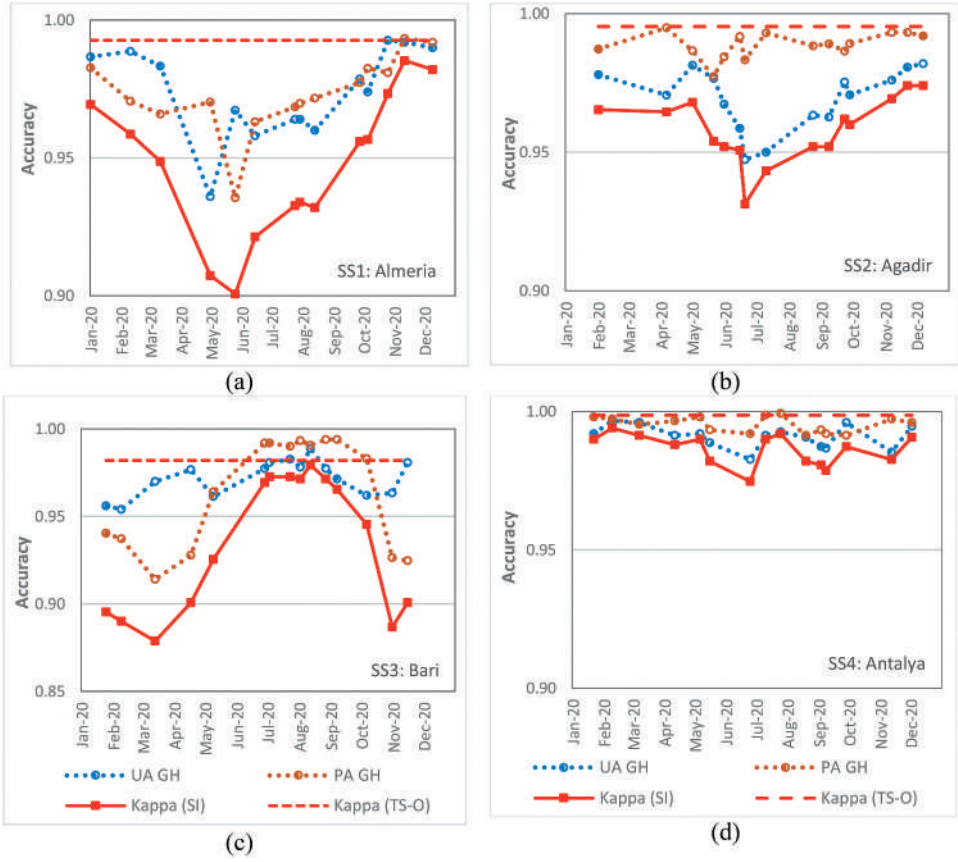

Figure 5. Object-based accuracy assessment based on 3000 objects (1500 GH and 1500 Non-GH): (a) SS1, Almería; (b) SS2, Agadir; (c) SS3, Bari; (d) SS4, Antalya. User's accuracy for Greenhouse class (UA GH). Producer's accuracy for Greenhouse class (PA GH). Kappa for each single image (Kappa (SI)). Kappa for time series using statistical features by objects (Kappa (TS-O)).

by PMLI, RPGI and MDI. The technique of vineyard monoculture in Bari (SS3) changed the ranking of spectral indices, now pointing to CSBI, Vi, FDI, PGI and NDBI as the most relevant.

Changes in the relative importance of the top six global indices (last column in Table 3) are depicted in Figure 4 over time for SS1 (Figure 4 (a)), SS2 (Figure 4(b)), SS3 (Figure 4(c)) and SS4 (Figure 4(d)). PGHI was the PCG detection index that had the best relative importance for all the recorded dates in SS1, SS2 and SS4. In the case of SS3, the relative importance of the tested indices was much more changeable and irregular.

Table 4 depicts the 14 most relevant statistical seasonal indices extracted from S2 time series for each study site. Again, their relative importance values are ordered in the last column according to the mean values for the four study sites. In this case, two statistical indices based on PGI (SD (PGI) and DIF (PGI)) and MAX (PGHI) stood out over the rest. MEAN (PGHI) presented very good relative importance values for all the study sites except for the case of SS3, which, as we indicated above, presents cultivation characteristics (monoculture vineyard) very different from those of the other study areas.

5.3 Object-based accuracy assessment

Figure 5 depicts the accuracy based on the 3000 selected objects (1500 GH and 1500 Non-GH) from the segmentations carried out for all the study sites. The accuracy figures were derived from DT models

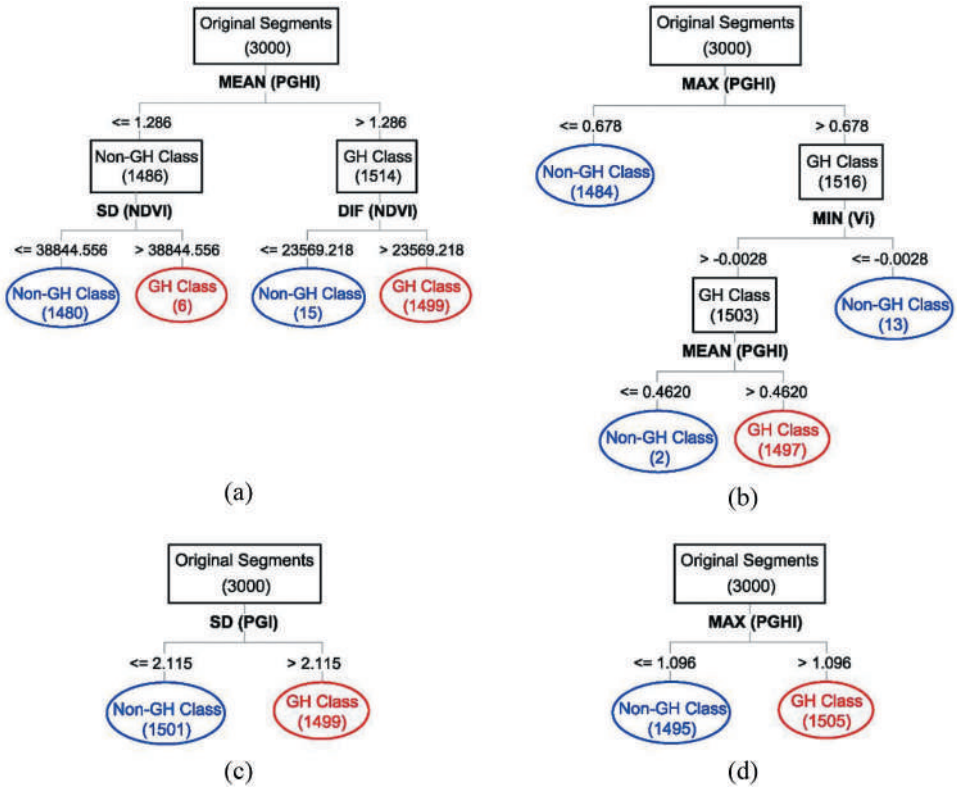

Figure 6. DT models proposed for GH and Non-GH classification based on statistical spectral indices from S2 time series: (a) SS1, Almería; (b) SS2, Agadir; (c) SS3, Bari; (d) SS4, Antalya.

computed on S2 single images (UA GH, PA GH, Kappa for each single image (Kappa (SI)) and Kappa for time series by objects (Kappa (TS-O)).

Figure 6 shows the four very simple DT models for PCG detection proposed for S2 time series based only on statistical indices for each study site. The first splits of these DT models used the following statistical features: MEAN (PGHI) in SS1 (Figure 6(a)), SD (PGI) in SS3 (Figure 6(c)), and MAX (PGHI) for SS2 and SS4. Only SS1 and SS2 presented secondary splits related to vegetation (e.g. SD (NDVI) and DIF (NDVI)) or other PCG indices (e.g. MIN (Vi)).

Looking again Figure 5, the accuracy values based on statistical seasonal features (Kappa (TS-O)) were higher than Kappa (SI) ones for all the study sites. The Kappa (TS-O) and OA time series values were 0.993 (OA = 99.63%), 0.995 (OA = 99.77%), 0.982 (OA = 99.10%) and 0.999 (OA = 99.93%) for SS1 (Figure 5(a)), SS2 (Figure 5(b)), SS3 (Figure 5(c)) and SS4 (Figure 5(d)), respectively.

Regarding the accuracy computed from S2 single images, Kappa (SI) values were varying over time. In Almería (SS1) and Agadir (SS2) the worst results were achieved in summer. Something similar, but much less marked, took place in Antalya (SS4), where the best accuracy values of Kappa (SI) were yielded. Just the opposite happened in Bari (SS3), where the best accuracy values were achieved in summer. It is worth noting that the greenhouses in Bari are covered with plastic sheets mainly in spring and summer. The omission error (PA GH) and commission error (UA GH) for the Greenhouse class achieved very good results, showing similar changes over time that Kappa.

5.4 Pixel-based accuracy assessment

Figure 7, Figure 8, Figure 9 and Figure 10 present both the manually digitized reference (ground truth zones) and the pixel-by-pixel (1 m GSD) comparison with the OBIA classification attained from applying the previously trained DT models (Figure 6) for each zone and study site. The Deimos-2 RGB orthoimages are also depicted in these figures for a better understanding the accuracy assessment.

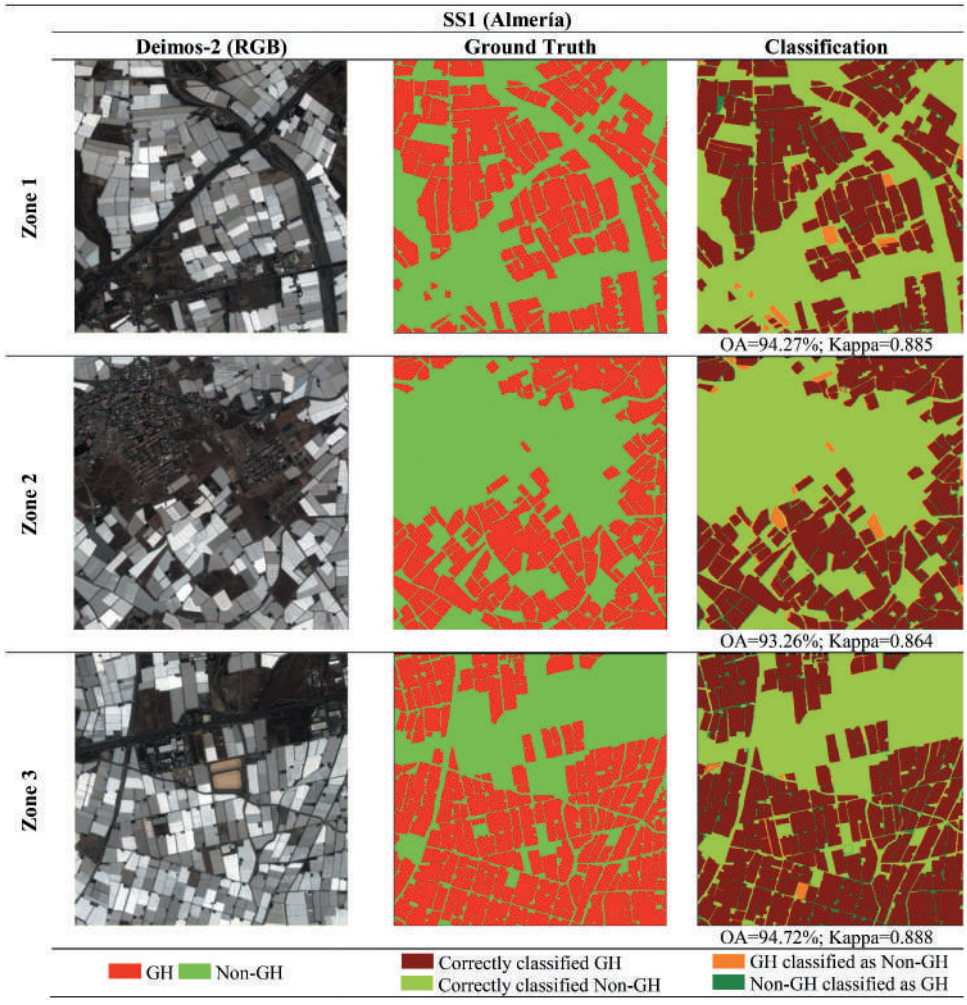

Figure 7. Pixel-based accuracy assessment for the DT models derived from S2 time series over the manually digitized Zones for SS1 (Almería).

Table 5. Comparison of mean values of accuracy measures for the three zones and study sites regarding the pixel-based accuracy assessment. Values in the same column followed by different superscript letters indicate significant differences at a significance level $p < 0.05$.

Study Site	OA	Kappa	UA GH	PA GH	UA Non-GH	PA Non-GH
SS1	94.09	0.879	94.34 [a]	94.23	94.03	93.34
SS2	92.27	0.840	87.16 [b]	94.93	96.17	90.27
SS3	92.77	0.809	80.33 [c]	94.15	95.89	92.39
SS4	92.17	0.834	85.08 [b]	97.19	97.98	87.94

The comparison maps between OBIA classification and ground truth show GH class in brown and Non-GH class in green. Moreover, dark green and orange colors highlight the misclassification errors. Pixels that are GH in the reference maps, but are classified as Non-GH in the classification maps, appear orange. On the other hand, pixels representing Non-GH in the reference maps, but are classified as GH, appear dark green in the classification maps. The accuracy measures for each zone and study area (OA and Kappa values) are also presented in Figure 7, Figure 8, Figure 9 and Figure 10.

Table 5 presents the statistical separation of mean values for the three zones of each study site corresponding to the accuracy measures of OA, Kappa, UA GH, PA GH, UA Non-GH and PA Non-GH. The accuracy results depicted in Table 5 did not show statistical significant differences between study sites ($p < 0.05$), with the only exception of UA GH. In this case, the best UA GH value was achieved in SS1, followed by SS2 and SS4 (statistically similar results), and placing last SS3.

6. Discussions

As already mentioned, several spectral indices for extraction of PCG, plastic-mulched areas or plastic litter in the marine environment have been

developed in the last 20 years, all of them providing good results for the classification of a wide variety of plastic elements located in different areas of the world. Hence, the idea of compare all of these indices for mapping PCG by applying the same methodology and in different PCG areas worldwide can be of great help for future research in this field.

Almost all the spectral indices tested in this work have already been tested for PCG detection, although the methodology followed was not always the same and, of course, the study sites and the type of PCG varied significantly. In that sense, Nemmaoui et al. (2018) tested basic spectral information features and several indices from S2 and Landsat 8 time series for mapping PCG in Almería (SS1) following a methodology very similar to that used in this work. They also worked with statistical features. Among these indices extracted from S2 images, there were ten out of the fourteen indices that have been also tested in this work (i.e. NDVI, NDBI, MDRP, MDLP, MDI, PMLI, Vi, PGI, RPGI and GDI). More recently, Ji et al. (2020) proposed the PGHI and CSBI indices to map PCG from Landsat 8 images using a similar OBIA approach in China. Aguilar, Jiménez-Lao, and Aguilar (2021) also applied the PI index in SS1 for detecting PCG from a single WorldView-3 image, resulting in a well-ranked index based on its relative importance in the classification when only the visible and near-infrared (VNIR) bands were used.

The accuracy values for the object-based assessment based on 3000 selected objects yielded impressive values, presenting OA values always higher than 99% from using statistical seasonal indices computed for each time series. Importantly, the accuracy of the classification was significantly improved by these statistical indices for all study sites (Figure 5). In this regards, Zillmann et al. (2014) had already used seasonal features successfully for mapping grassland, and Aguilar et al. (2016) and Nemmaoui et al. (2018) to map PCG. These works reported that seasonal statistics were more robust over time than snapshot values derived from single images.

The classification accuracy values achieved in the S2 single images resulted to be very variable, being generally worse in summer for the three study sites devoted to growing vegetables (SS1, SS2 and SS4). Note that PCG are whitewashed in the summer season due to the excessive radiation. Moreover, some indices, such as PGI proposed by Yang et al. (2017), are very sensitive to the vegetation beneath plastic cover and, when PCG are often empty in summer, they are more ineffective. It is important to note that greenhouses in Bari are usually covered with plastic sheets mainly in spring and summer. Because of that, the spectral indices for mapping PCG worked better in this period. Plastic film covers are used in viticulture to anticipate the ripening period of early and very early grape varieties (early-covering) or to delay the ripening period (late-covering) on medium-late or late varieties. In the first case, both vineyard top and laterals are protected with plastic films from the end of winter until the harvest. In the late-covering, the covering period coincides with the veraison phase (before the rains of late summer) and, in this case, the plastic film is applied only on the top (Novello and de Palma 2008). Furthermore, some vineyards are only covered with hail nets to protect them from the weather (Tarantino and Figorito 2012). In that sense, the variety of plastic materials used (mainly nets and plastic sheets) as well as the heterogeneity of periods in which vineyards are covered throughout the year can explain the high variability and inconsistency of the classification accuracy values and the rank of relative importance for the indices tested in SS3. It is important to point out that the DT models computed from S2 single images only presented two or three terminal nodes in SS1, SS2 and SS4, but this number increased to 7 for SS3 in some winter months.

Leaving aside SS3, PGHI can be qualified the best spectral index for mapping PCG when using S2 single images. In fact, that index had the maximum relative importance for all the single images and study sites (Table 3). In the threshold model built by Ji et al. (2020), the split values for PGHI were ranging from 0.43 to 0.68 in four cases (two different regions and two years). In the DT models computed in this work for S2 single images, the first split presented mean values of 1.12, 0.52 and 0.71 for SS1, SS2 and SS4, respectively. Definitely, the cutoff value of this index depended on the study area where it was applied, so it should be calculated in a supervised way for each case.

Also in Table 3, and looking at the vegetation cover of different study sites in Figure 1, it is easy to understand why NDVI index resulted to be most important

for SS3 and SS4 which included most green areas, while least important for SS1 and SS2 with least vegetation. Regarding CSBI index, proposed to discriminate the color steel buildings, its importance was the highest working on SS3, which presented the highest proportion of urban areas.

Regarding the importance of statistical indices, SD (PGI) achieved the best global results. Nemmaoui et al. (2018) reported SD (PGI) as the most significant statistical seasonal index (first split in the DT model) for time series from S2 and Landsat 8. In this work, and working with S2 single images, PGI was not among the top six indices (Figure 4), although SD (PGI) showed a very good performance when the entire time series and statistical indices were considered. It is likely due to its high range of variability over time to discriminate between GH and Non-GH classes (Nemmaoui et al. 2018). Finally, SD (PGI) appeared only in the DT model for Bari (Figure 6(c)) showing a threshold value of 2.115. Nemmaoui et al. (2018) reported different thresholds for S2 (2.0) and for Landsat 8 (0.8). Statistical indices based on PGHI were located in the first split of SS1 (MEAN (PGHI)), and SS2 and SS4 (MAX (PGHI)), although none of these thresholds provided robust results (Figure 6).

When performing the OBIA classification using the DT models shown in Figure 6, the accuracy assessments based on pixels (Figure 7, Figure 8, Figure 9, Figure 10 and Table 5) were quite worse than those based on objects (Figure 5). In fact, the misclassification problems due to errors in the segmentation step were avoided in the object-based accuracy assessment, where 3000 meaningful objects were selected as ground truth. In that sense, the OA mean values using the pixel-based accuracy assessment of 94.09%, 92.27%, 92.77% and 92.17% computed for SS1, SS2,

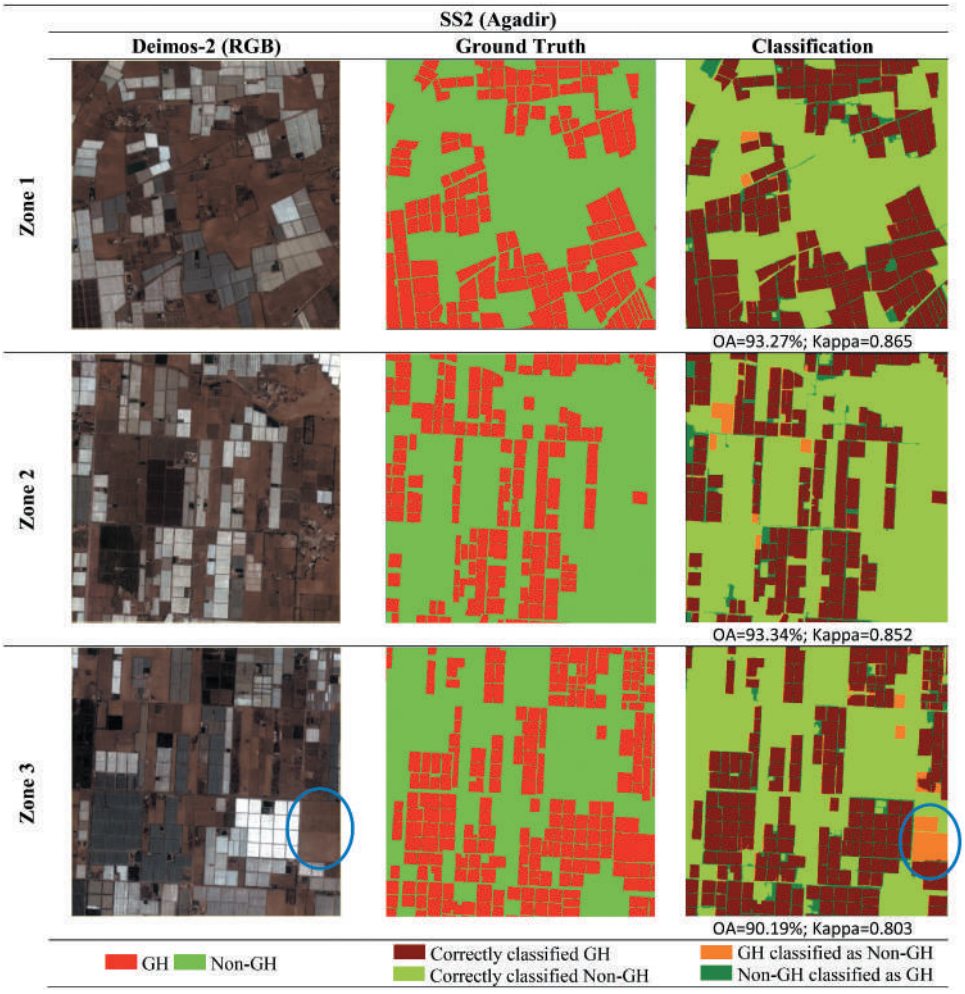

Figure 8. Pixel-based accuracy assessment for the DT models derived from S2 time series over the manually digitized Zones for SS2 (Agadir).

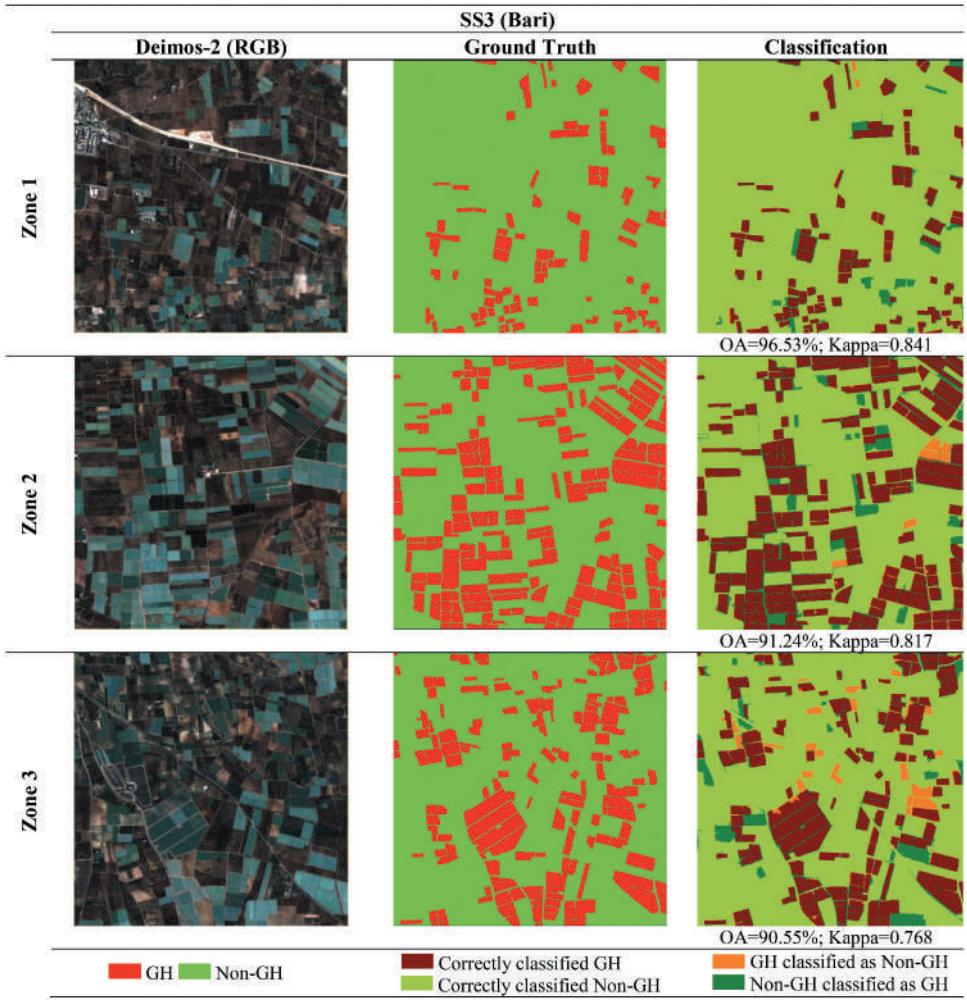

Figure 9. Pixel-based accuracy assessment for the DT models derived from S2 time series over the manually digitized Zones for SS3 (Bari).

SS3 and SS4, respectively, turns out to be more realistic accuracy results than those calculated using previously selected objects as reference. Following a similar methodology, OA values in SS1 of 93.97% and 92.65% were achieved by Nemmaoui et al. (2018) using S2 and Landsat 8 time series, respectively. Moreover, Aguilar et al. (2016) achieved OA of 92.3% (2014) and 92.42% (2015) for two annual time series, of pansharpened Landsat 8 images, also in SS1. In other studies, very changeable values of OA were reported depending on the methodology followed. For instance, OA values of 89.6% and 92.6% were reported by Feng et al. (2021) mapping PCG and mulching films from VHR remote sensing imagery based on a dilated and non-local convolutional neural network in China and Saudi Arabia. Sun et al. (2021) reported an OA of 91.38% using two-temporal S2 images and 1D-CNN deep learning approach in China for mapping PCG. Ji et al. (2020) reached an impressive OA values of 98.49% and 99.93% working on Landsat 8 images and using an OBIA approach and a threshold model for detecting PCG. In this last work, 18,000 points were randomly created for accuracy assessment.

Looking at Figure 7, Figure 8, Figure 9 and Figure 10, a reduced number of objects were misclassified showing orange or dark green colors in the classification maps of the different study sites. For instance, in Figure 8 and highlighted by blue ellipses, it can be seen an area without PCG over the Deimos-2 orthoimage, although in the ground truth this group of agricultural parcels

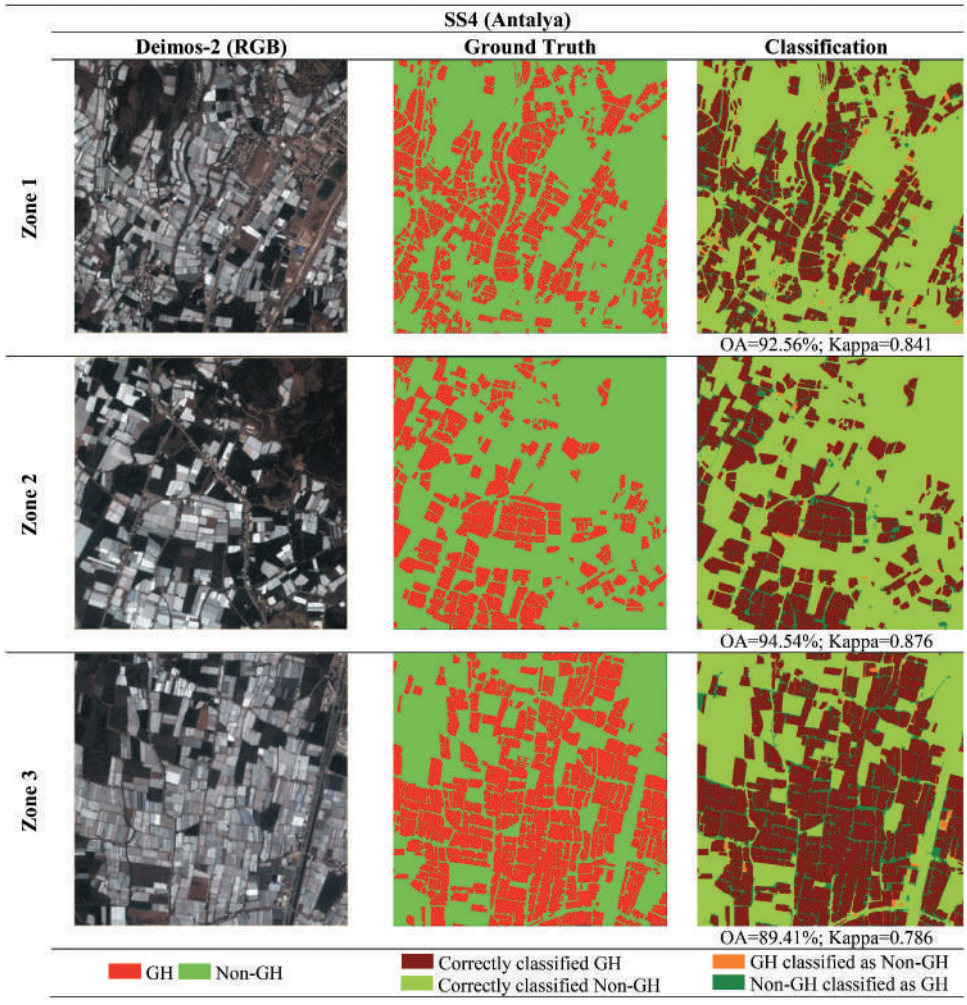

Figure 10. Pixel-based accuracy assessment for the DT models derived from S2 time series over the manually digitized Zones for SS4 (Antalya).

appeared as GH. Really, new PCG were covered in plastic only in the two last S2 images of the time series in Agadir. Therefore, statistical seasonal features computed for each index and object were not very robust.

However, there were many pixels badly classified due to some errors made in the segmentation stage. We can also see that another important source of error in dark green was located at narrow streets between greenhouses, where Non-GH objects were classified as GH due to the presence of mixed pixels (Wu et al. 2016). In this context, Ji et al. (2020) included two shape indices in their threshold model to reject irregular and elongated objects as PCG.

One of the main problems for mapping PCG is usually related to distinguish PCG from bright white buildings. For that, Ji et al. (2020) proposed PGHI. This index is based on the low reflectance values of SWIR2 band relative to Blue band in PCG, while in white buildings the values of SWIR2 are higher than the Blue ones. In addition, the variation of NDVI due to the crops that are growing underneath the plastic films over time is other useful tool to discriminate

PCG and buildings. In this regard, SD (NDVI) was one of the seasonal indices that was presented in the DT for the SS1 in Figure 6.

7. Conclusions

In this study, a fair comparison between 14 spectral indices was carried out in four PCG study sites around the world, and over an entire year. The OBIA approach was based on the combined use of VHR satellite data (Deimos-2 pansharpened images) to address the segmentation process and S2 time series to compute the tested spectral indices.

Deimos-2 pansharpened images were used to get the optimal segmentation for individual PCG by using MRS algorithm and the modified ED2 metric. The attained segmentations had a very good visual quality with respect to PCG.

Using the previously attained objects, DT models were used to determine the best object-based indices for PCG mapping in Almería, Agadir, Bari and Antalya, working on both S2 single images (testing single spectral indices over time) and S2 time series (using statistical seasonal indices). The test with S2 single images provided information about the variation of the importance of the 14 indices tested and their accuracy over time in each study site. Furthermore, the statistical indices for each S2 time series achieved the best OA values of 94.09%, 92.27%, 92.77% and 92.17% for Almería, Agadir, Bari and Antalya, respectively.

PGHI stood out among all the indices tested in the study areas dedicated to growing vegetables (i.e. Almería, Agadir and Antalya), being the first split of all the individual DT models computed for each S2 single image. It is important to note that the two indices related to classify marine plastic debris (PI and FDI) did not give good results working on PCG. Regarding the statistical indices, MAX (PGHI), MEAN (PGHI) and SD (PGI) were the most discriminating indices.

To the best knowledge of the authors, this is the first work that deals with the classification of PCG from S2 time series in several countries. Although each study site presented unique characteristics, many of them presented some similarities when they were put through these tests. In this way, Bari, with a monoculture in vineyard, presented the worst and the most irregular results. On the other hand, Almería, Agadir and Antalya, the three study sites dedicated to the cultivation of vegetables, achieved better and more similar results.

Acknowledgements

This research was funded by Spanish Ministry for Science, Innovation and Universities (Spain) and the European Union (European Regional Development Fund, ERDF) funds, grant number RTI2018-095403-B-I00 This study takes part in the general research lines promoted by the Agrifood Campus of International Excellence ceiA3.

Disclosure statement

No potential conflict of interest was reported by the author(s).

Funding

This work was supported by the Ministerio de Ciencia, Innovación y Universidades, Spain [RTI2018-095403-B-I00].

ORCID

Manuel A. Aguilar http://orcid.org/0000-0003-0404-9875
Fernando J. Aguilar http://orcid.org/0000-0002-5144-6411
Eufemia Tarantino http://orcid.org/0000-0002-2468-0771

Data availability

The data that support the findings of this study are available on request from the corresponding author (Manuel A. Aguilar, email: maguilar@ual.es). The AssesSeg code are available in: https://w3.ual.es/Proyectos/GreenhouseSat/index_archivos/links.htm

References

Agüera, F., M. A. Aguilar, and F. J. Aguilar. 2006. "Detecting Greenhouse Changes from QB Imagery on the Mediterranean Coast." *International Journal of Remote Sensing* 27 (21): 4751–4761. doi:10.1080/01431160600702681.

Agüera, F., F. J. Aguilar, and M. A. Aguilar. 2008. "Using Texture Analysis to Improve Per-pixel Classification of Very High Resolution Images for Mapping Plastic Greenhouses." *ISPRS Journal of Photogrammetry and Remote Sensing* 63 (6): 635–646. doi:10.1016/j.isprsjprs.2008.03.003.

Aguilar, M. A., F. Bianconi, F. J. Aguilar, and I. Fernández. 2014. "Object-Based Greenhouse Classification from GeoEye-1 and WorldView-2 Stereo Imagery." *Remote Sensing* 6 (5): 3554–3582. doi:10.3390/rs6053554.

Aguilar, M. A., R. Jiménez-Lao, and F. J. Aguilar. 2021. "Evaluation of Object-Based Greenhouse Mapping Using WorldView-3 VNIR and SWIR Data: A Case Study from Almería (Spain)." *Remote Sensing* 13 (11): 2133. doi:10.3390/rs13112133.

Aguilar, M. A., R. Jiménez-Lao, A. Nemmaoui, and F. J. Aguilar. 2020b. "Geometric Accuracy Assessment of Deimos-2 Panchromatic Stereo Pairs: Sensor Orientation and Digital Surface Model Production." *Sensors* 20 (24): 7234. doi:10.3390/s20247234.

Aguilar, M. A., R. Jiménez-Lao, A. Nemmaoui, F. J. Aguilar, D. Koc-San, E. Tarantino, and M. Chourak. 2020a. "Evaluation of the Consistency of Simultaneously Acquired Sentinel-2 and Landsat 8 Imagery on Plastic Covered Greenhouses." *Remote Sensing* 12 (12): 2015. doi:10.3390/rs12122015.

Aguilar, M. A., A. Nemmaoui, F. J. Aguilar, A. Novelli, and A. M. García Lorca. 2017. "Improving Georeferencing Accuracy of Very High Resolution Satellite Imagery Using Freely Available Ancillary Data at Global Coverage." *International Journal of Digital Earth* 10 (10): 1055–1069. doi:10.1080/17538947.2017.1280549.

Aguilar, M. A., A. Nemmaoui, A. Novelli, F. J. Aguilar, and A. García Lorca. 2016. "Object-Based Greenhouse Mapping Using Very High Resolution Satellite Data and Landsat 8 Time Series." *Remote Sensing* 8 (6): 513. doi:10.3390/rs8060513.

Aguilar, M. A., A. Novelli, A. Nemmaoui, F. J. Aguilar, A. M. García Lorca, and O. González-Yebra. 2018. "Optimizing Multiresolution Segmentation for Extracting Plastic Greenhouses from Worldview-3 Imagery." In: *International Conference on Intelligent Interactive Multimedia Systems and Services*, Vilamoura (Portugal). Springer, pp. 31–40. doi:10.1007/978-3-319-59480-4_4.

Aguilar, M. A., A. Vallario, F. J. Aguilar, A. M. García Lorca, and C. Parente. 2015. "Object-Based Greenhouse Horticultural Crop Identification from Multi-Temporal Satellite Imagery: A Case Study in Almeria, Spain." *Remote Sensing* 7 (6): 7378–7401. doi:10.3390/rs70607378.

Arcidiacono, C., and S. M. C. Porto. 2011. "Improving Per-pixel Classification of Crop-shelter Coverage by Texture Analyses of High-resolution Satellite Panchromatic Images." *Journal of Agricultural Engineering* 4: 9–16. doi:10.4081/jae.2011.4.9.

Baatz, M., and M. Schäpe. 2000. "Multiresolution Segmentation —An Optimization Approach for High Quality Multi-Scale Image Segmentation." In *Angewandte Geographische Informations-Verarbeitung XII*, edited by J. Strobl, T. Blaschke, and G. Griesebner, 12–23. Vol. 2000. Karlsruhe, Germany: Wichmann Verlag.

Balcik, F. B., G. Senel, and C. Goksel. 2020. "Object-Based Classification of Greenhouses Using Sentinel-2 MSI and SPOT-7 Images: A Case Study from Anamur (Mersin), Turkey." *IEEE Journal of Selected Topics in Applied Earth Observations and Remote Sensing* 13: 2769–2777. doi:10.1109/JSTARS.2020.2996315.

Berk, A., L. S. Bernstein, G. P. Anderson, P. K. Acharya, D. C. Robertson, J. H. Chetwynd, and S. M. Adler-Golden. 1998. "MODTRAN Cloud and Multiple Scattering Upgrades with Application to AVIRIS." *Remote Sensing of Environment* 65 (3): 367–375. doi:10.1016/S0034-4257(98)00045-5.

Biermann, L., D. Clewley, V. Martinez-Vicente, K. Topouzelis, and A. Elbe-Bürger. 2020. "Finding Plastic Patches in Coastal Waters Using Optical Satellite Data." *Scientific Reports* 10 (1): 1–10. doi:10.1038/s41598-020-62298-z.

Breiman, L., J. H. Friedman, R. A. Olshen, and C. I. Stone. 1984. *Classification and Regression Trees*, 1984. Boca Raton FL: Chapman & Hall/CRC Press.

Carvajal, F., F. Agüera, F. J. Aguilar, and M. A. Aguilar. 2010. "Relationship between Atmospheric Correction and Training Site Strategy with respect to Accuracy of Greenhouse Detection Process from Very High Resolution Imagery." *International Journal of Remote Sensing* 31 (11): 2977–2994. doi:10.1080/01431160902946580.

Congalton, R. G. 1991. "A Review of Assessing the Accuracy of Classifications of Remotely Sensed Data." *Remote Sensing of Environment* 37 (1): 35–46. doi:10.1016/0034-4257(91)90048-B.

Cuesta Roble Consulting 2019. "World Greenhouse Vegetable Statistics - 2019 Updates." https://www.cuestaroble.com/statistics.html

eCognition. 2019. *Reference Book: Trimble eCognition Developer for Windows Operating System*, D–80636. Vol. 126. Munich, Germany: Trimble Germany GmbH, Arnulfstrasse.

Espi, E., A. Salmerón, A. Fontecha, Y. García, and A. I. Real. 2006. "Plastic Films for Agricultural Applications." *Journal of Plastic Film & Sheeting* 22 (2): 85–102. doi:10.1177/8756087906064220.

FAO 2021. "Assessment of Agricultural Plastics and Their Sustainability: A Call for Action." Rome. doi: 10.4060/cb7856en.

Feng, Q., B. Niu, B. Chen, Y. Ren, D. Zhu, J. Yang, J. Liu, C. Ou, and B. Li. 2021. "Mapping of Plastic Greenhouses and Mulching Films from Very High Resolution Remote Sensing Imagery Based on a Dilated and Non-local Convolutional Neural Network." *International Journal of Applied Earth Observation and Geoinformation* 102: 102441. doi:10.1016/j.jag.2021.102441.

Foley, J. A., N. Ramankutty, K. A. Brauman, S. C. E, J. S. Gerber, M. Johnston, N. D. Mueller, et al. 2011. "Solutions for a Cultivated Planet." *Nature* 478 (7369): 337–342. doi:10.1038/nature10452.

Garnaud, J. C. 2000. "Plasticulture Magazine: A Milestone for A History of Progress in Plasticulture." *Plasticulture* 119: 30–43.

González-Yebra, Ó., M. A. Aguilar, A. Nemmaoui, and F. J. Aguilar. 2018. "Methodological Proposal to Assess Plastic Greenhouses Land Cover Change from the Combination of Archival Aerial Orthoimages and Landsat Data." *Biosystems Engineering* 175: 36–51. doi:10.1016/j.biosystemseng.2018.08.009.

Hasituya, Z., and Z. Chen. 2017. "Mapping Plastic-Mulched Farmland with Multi-Temporal Landsat-8 Data." *Remote Sensing* 9 (6): 557. doi:10.3390/rs9060557.

Hao, P., Z. Chen, H. Tang, D. Li, and H. Li. 2019. "New Workflow of Plastic-Mulched Farmland Mapping Using Multi-Temporal Sentinel-2 Data." *Remote Sensing* 11 (11): 1353. doi:10.3390/rs11111353.

Hasituya, Z., F. L. Chen, Y. Hu, and H. Yuncai. 2020. "Mapping Plastic-mulched Farmland by Coupling Optical and Synthetic Aperture Radar Remote Sensing." *International Journal of Remote Sensing* 41 (20): 7757–7778. doi:10.1080/01431161.2020.1763510.

Hasituya, Z., Z. L. Chen, F. Li, and L. Fei. 2021. "Potential of Pléiades and Radarsat-2 Data for Mapping Plastic-Mulched Farmland Using Object-Based Image Analysis." *Canadian Journal of Remote Sensing* 47 (4): 607–620. doi:10.1080/07038992.2021.1946384.

Ibrahim, E., and A. Gobin. 2021. "Sentinel-2 Recognition of Uncovered and Plastic Covered Agricultural Soil." *Remote Sensing* 13 (21): 4195. doi:10.3390/rs13214195.

Jakab, B., B. van Leeuwen, and T. Zalán. 2021. "Detection of Plastic Greenhouses Using High Resolution RGB Remote Sensing Data and Convolutional Neural Network." *Journal of Environmental Geography* 14 1–2: 38–46. doi:10.2478/jengeo-2021-0004.

Jambeck, J. R., R. Geyer, C. Wilcox, T. R. Siegler, M. Perryman, A. Andrady, R. Narayan, and K. L. Law. 2015. "Plastic Waste Inputs from Land into the Ocean." *Marine Pollution* 347: 768–771. doi:10.1126/science.1260352.

Jensen, M. H., and A. J. Malter. 1995. *Protected Agriculture: A Global Review*. Vol. 253. Washington DC: World Bank Publications.

Ji, L., L. Zhang, Y. Shen, X. Li, W. Liu, Q. Chai, R. Zhang, and D. Chen. 2020. "Object-Based Mapping of Plastic Greenhouses with Scattered Distribution in Complex Land Cover Using Landsat 8 OLI Images: A Case Study in Xuzhou, China." *Journal of the Indian Society of Remote Sensing* 48 (2): 287–303. doi:10.1007/s12524-019-01081-8.

Koc-San, D. 2013. "Evaluation of Different Classification Techniques for the Detection of Glass and Plastic Greenhouses from WorldView-2 Satellite Imagery." *Journal of Applied Remote Sensing* 7 (1): 073553. doi:10.1117/1.JRS.7.073553.

Li, M., Z. Zhang, L. Lei, X. Wang, and X. Guo. 2020. "Agricultural Greenhouses Detection in High-Resolution Satellite Images Based on Convolutional Neural Networks: Comparison of Faster R-CNN, YOLO V3 and SSD." *Sensors* 20 (17): 4938. doi:10.3390/s20174938.

Liu, Y., L. Biana, Y. Menga, H. Wanga, S. Zhanga, Y. Yanga, X. Shaoa, and B. Wang. 2012. "Discrepancy Measures for Selecting Optimal Combination of Parameter Values in Object-based Image Analysis." *ISPRS Journal of Photogrammetry and Remote Sensing* 68: 144–156. doi:10.1016/J.ISPRSJPRS.2012.01.007.

Lu, L., L. Di, and Y. Ye. 2014. "A Decision-Tree Classifier for Extracting Transparent Plastic-Mulched Landcover from Landsat-5 TM Images." *IEEE Journal of Selected Topics in Applied Earth Observations and Remote Sensing* 7 (11): 4548–4558. doi:10.1109/JSTARS.2014.2327226.

Lu, L., Y. Tao, and L. Di. 2018. "Object-Based Plastic-Mulched Landcover Extraction Using Integrated Sentinel-1 and Sentinel-2 Data." *Remote Sensing* 10 (11): 1820. doi:10.3390/rs10111820.

Ma, A., D. Chen, Y. Zhong, Z. Zheng, and L. Zhang. 2021. "National-scale Greenhouse Mapping for High Spatial Resolution Remote Sensing Imagery Using A Dense Object Dual-task Deep Learning Framework: A Case Study of China." *ISPRS Journal of Photogrammetry and Remote Sensing* 181: 279–294. doi:10.1016/j.isprsjprs.2021.08.024.

Nemmaoui, A., M. A. Aguilar, F. J. Aguilar, A. Novelli, and A. García Lorca. 2018. "Greenhouse Crop Identification from Multi-Temporal Multi-Sensor Satellite Imagery Using Object-Based Approach: A Case Study from Almería (Spain)." *Remote Sensing* 10 (11): 1751. doi:10.3390/rs10111751.

Novelli, A., M. A. Aguilar, F. J. Aguilar, A. Nemmaoui, and E. Tarantino. 2017. "AssesSeg—A Command Line Tool to Quantify Image Segmentation Quality: A Test Carried Out in Southern Spain from Satellite Imagery." *Remote Sensing* 9 (1): 40. doi:10.3390/rs9010040.

Novelli, A., M. A. Aguilar, A. Nemmaoui, F. J. Aguilar, and E. Tarantino. 2016. "Performance Evaluation of Object Based Greenhouse Detection from Sentinel-2 MSI and Landsat 8 OLI Data: A Case Study from Almería (Spain)." *International Journal of Applied Earth Observation and Geoinformation* 52: 403–411. doi:10.1016/j.jag.2016.07.011.

Novelli, A., and E. Tarantino. 2015. "Combining Ad Hoc Spectral Indices Based on Landsat-8 OLI/TIRS Sensor Data for the Detection of Plastic Cover Vineyard." *Remote Sensing Letters* 6 (12): 933–941. doi:10.1080/2150704X.2015.1093186.

Novello, V., and L. de Palma. 2008. "Growing Grapes under Cover." *Acta Horticulturae* 785 (785): 353–362. doi:10.17660/ActaHortic.2008.785.44.

Ou, C., J. Yang, Z. Du, Y. Liu, Q. Feng, and D. Zhu. 2020. "Long-Term Mapping of a Greenhouse in a Typical Protected Agricultural Region Using Landsat Imagery and the Google Earth Engine." *Remote Sensing* 12 (1): 55. doi:10.3390/rs12010055.

Peña-Barragán, J. M., P. A. Gutiérrez, C. Hervás-Martínez, J. Six, R. E. Plant, and F. López-Granados. 2014. "Object-based Image Classification of Summer Crops with Machine Learning Methods." *Remote Sensing* 6 (6): 5019–5041. doi:10.3390/rs6065019.

Peña-Barragán, J. M., M. K. Ngugi, R. E. Plant, and J. Six. 2011. "Object-based Crop Identification Using Multiple Vegetation Indices, Textural Features and Crop Phenology." *Remote Sensing of Environment* 115 (6): 1301–1316. doi:10.1016/j.rse.2011.01.009.

Perilla, G. A., and J. F. Mas. 2019. "High-resolution Mapping of Protected Agriculture in Mexico, through Remote Sensing Data Cloud Geoprocessing." *European Journal of Remote Sensing* 52 (1): 532–541. doi:10.1080/22797254.2019.1686430.

Picuno, P., A. Tortora, and R. L. Capobianco. 2011. "Analysis of Plasticulture Landscapes in Southern Italy through Remote Sensing and Solid Modelling Techniques." *Landscape and Urban Planning* 100 (1–2): 45–56. doi:10.1016/j.landurbplan.2010.11.008.

RaboResearch. 2018. *The 2018 World Vegetable Map*. Rabobank Research Food & Agribusiness. https://research.rabobank.com/far/en/sectors/regional-food-agri/world_vegetable_map_2018.html

Rouse, J. W., Jr., R. H. Haas, J. A. Schell, and D. W. Deering. 1973. "Monitoring Vegetation Systems in the Great Plains with ERTS." In: *Proceedings of the Third ERTS Symposium*, NASA SP-351, Washington, DC, USA, 10-14 December 1973.

The Royal Society. 2009. *Reaping the Benefits: Science and the Sustainable Intensification of Global Agriculture*. London: Royal Society. https://royalsociety.org/topics-policy/publications/2009/reaping-benefits/

Salas, E. A. L., and G. M. Henebry. 2012. "Separability of Maize and Soybean in the Spectral Regions of Chlorophyll and Carotenoids Using the Moment Distance Index." *Israel Journal of Plant Sciences* 60 (1): 65–76. doi:10.1560/IJPS.60.1-2.65.

Shi, L., X. Huang, T. Zhong, and H. Taubenböck. 2020. "Mapping Plastic Greenhouses Using Spectral Metrics Derived from GaoFen-2 Satellite Data." *IEEE Journal of Selected Topics in Applied Earth Observations and Remote Sensing* 13: 49–59. doi:10.1109/JSTARS.2019.2950466.

Song, X.-P., P. V. Potapov, A. Krylov, L. King, C. M. Di Bella, A. Hudson, A. Khan, B. Adusei, S. V. Stehman, and M. C. Hansen. 2017. "National-scale Soybean Mapping and Area Estimation in the United States Using Medium Resolution Satellite Imagery and Field Survey." *Remote Sensing of Environment* 190: 383–395. doi:10.1016/J.RSE.2017.01.008.

Stumpf, A., D. Michéa, and J.-P. Malet. 2018. "Improved Co-Registration of Sentinel-2 and Landsat-8 Imagery for Earth Surface Motion Measurements." *Remote Sensing* 10 (2): 160. doi:10.3390/rs10020160.

Sun, H., L. Wang, R. Lin, Z. Zhang, and B. Zhang. 2021. "Mapping Plastic Greenhouses with Two-Temporal Sentinel-2 Images and 1D-CNN Deep Learning." *Remote Sensing* 13 (14): 2820. doi:10.3390/rs13142820.

Tarantino, E., and B. Figorito. 2012. "Mapping Rural Areas with Widespread Plastic Covered Vineyards Using True Color Aerial Data." *Remote Sensing* 4 (7): 1913–1928. doi:10.3390/rs4071913.

Themistocleous, K., C. Papoutsa, S. Michaelides, and D. Hadjimitsis. 2020. "Investigating Detection of Floating Plastic Litter from Space Using Sentinel-2 Imagery." *Remote Sensing* 12 (16): 2648. doi:10.3390/rs12162648.

Tian, J., and D. M. Chen. 2007. "Optimization in Multi-scale Segmentation of High Resolution Satellite Images for Artificial Feature Recognition." *International Journal of Remote Sensing* 28 (20): 4625–4644. doi:10.1080/01431160701241746.

Vieira, M. A., A. R. Formaggio, C. D. Rennó, C. Atzberger, D. A. Aguiar, and M. P. Mello. 2012. "Object Based Image Analysis and Data Mining Applied to a Remotely Sensed Landsat Time-series to Map Sugarcane over Large Areas." *Remote Sensing of Environment* 123: 553–562. doi:10.1016/J.RSE.2012.04.011.

Wu, C. F., J. S. Deng, K. Wang, L. G. Ma, and A. R. S. Tahmassebi. 2016. "Object-based Classification Approach for Greenhouse Mapping Using Landsat-8 Imagery." *International Journal of Agricultural and Biological Engineering* 9: 79–88. doi:10.3965/j.ijabe.20160901.1414.

Xiong, Y., Q. Zhang, X. Chen, A. Bao, J. Zhang, and Y. Wang. 2019. "Large Scale Agricultural Plastic Mulch Detecting and Monitoring with Multi-Source Remote Sensing Data: A Case Study in Xinjiang, China." *Remote Sensing* 11 (18): 2088. doi:10.3390/rs11182088.

Yang, D., J. Chen, Y. Zhou, X. Chen, X. Chen, and X. Cao. 2017. "Mapping Plastic Greenhouse with Medium Spatial Resolution Satellite Data: Development of a New Spectral Index." *ISPRS Journal of Photogrammetry and Remote Sensing* 128: 47–60. doi:10.1016/j.isprsjprs.2017.03.002.

Zambon, M., R. Lawrence, A. Bunn, and S. Powell. 2006. "Effect of Alternative Splitting Rules on Image Processing Using Classification Tree Analysis." *Photogrammetric Engineering & Remote Sensing* 1 (1): 25–30. doi:10.14358/PERS.72.1.25.

Zha, Y., J. Gao, and S. Ni. 2003. "Use of Normalized Difference Built-up Index in Automatically Mapping Urban Areas from TM Imagery." *International Journal of Remote Sensing* 24 (3): 583–594. doi:10.1080/01431160304987.

Zhang, X., B. Cheng, J. Chen, and C. Liang. 2021. "High-Resolution Boundary Refined Convolutional Neural Network for Automatic Agricultural Greenhouses Extraction from GaoFen-2 Satellite Imageries." *Remote Sensing* 13 (21): 4237. doi:10.3390/rs13214237.

Zhao, G., J. Li, T. Li, and T. Warner. 2004. "Utilizing Landsat TM Imagery to Map Greenhouses in Qingzhou, Shandong Province, China." *Pedosphere* 14 (3): 363–369.

Zillmann, E., A. Gonzalez, E. J. Montero Herrero, J. van Wolvelaer, T. Esch, M. Keil, H. Weichelt, and A. M. Garzón. 2014. "Pan-European Grassland Mapping Using Seasonal Statistics from Multisensor Image Time Series." *IEEE Journal of Selected Topics in Applied Earth Observations and Remote Sensing* 7 (8): 3461–3472. doi:10.1109/JSTARS.2014.2321432.